PRAMANA
— journal of
physics

Vol. 58, No. 2
February 2002
pp. 293–311

Spin and charge transport in the presence of spin-orbit interaction

T P PAREEK and P BRUNO
Max-Planck-Institute für Mikrostrukturphysik, Weinberg 2, D-06120 Halle, Germany

Abstract. We present the study of spin and charge transport in nanostructures in the presence of spin-orbit (SO) interaction. Single band tight binding Hamiltonians for Elliot–Yafet and Rashba SO interaction are derived. Using these tight binding Hamiltonians and spin resolved Landauer–Büttiker formula, spin and charge transport is studied. Specifically numerical results are presented for a new method to perform magnetic scanning tunneling microscopy with non-magnetic tip but in the presence of Elliot–Yafet SO interaction. The spin relaxation phenomena in two-dimensional electron gas in the presence of Rashba SO interaction are studied and contrary to naive expectation, it is shown that disorder helps to reduce spin relaxation.

Keywords. Spin-orbit interaction; two-dimensional electron gas; Landauer–Büttiker formula.

PACS Nos 61.16.Ch; 73.40.Gk; 75.30.Pd; 75.60.Ch

1. Introduction

The usual electronic devices based on semiconductor relies on the electronic charge distribution which are easily shaped and controlled to make logic gates. Since the gate switching and intercommunication rates limits the device speed, efforts to improve computational power and speed have led researchers to explore the possibility to use electron spin, rather than its charge as the basis of new electronic devices dubbed as 'spintronics' [1]. The new field of *spintronics* exploits the ability of conduction electrons in metals and semiconductors to carry spin-polarized current. However, for the success of electronic devices based on electron spin it is essential that electron remembers its spin polarization over the length of the device. This is especially important for electronic applications, because if spin relaxes too fast, the distance traversed by electron without losing its spin will be too short to serve any practical purpose. In view of this a lot of effort went into identifying different mechanism of spin relaxation and reducing them. In semiconductor devices the most important interaction which causes spin relaxation is spin-orbit (SO) interaction. The spin-orbit interaction couples the spin degree of freedom to the spatial motion of the electron, which significantly influences the transport properties of solids. Among important consequences of spin-orbit interaction on electronic transport which have been widely investigated in the past let us mention the anomalous Hall effect and anisotropic magnetoresistance of ferromagnets, as well as weak antilocalization in disordered conductors.

The spin-orbit interaction is responsible for various spin-relaxation mechanisms of conduction in metals and semi-conductors. In the Elliott–Yafet mechanism [2], spin-relaxation is due to random spin-flip scattering due to spin-orbit interaction at impurities. In the D'yakonov–Perel mechanism [3], spin-relaxation arises from spin-precession of electrons due to the spin-orbit interaction between two scattering events. The Bir–Aronov–Pikus [4] involves the exchange interaction with holes, which in turn rapidly relaxes their spin by spin-orbit interaction. For a recent review see ref. [5].

The spin-orbit interaction is a relativistic correction to the non-relativistic Pauli equation, which arises as a combination of two effects: (i) the effective magnetic field experienced in its rest frame by an electron moving in an electric field and (ii) the Thomas precession of the rest frame of an accelerated electron. It is derived from the Dirac equation and expressed as

$$H_{\mathrm{SO}} = \frac{\hbar}{4m_0^2c^2}(\nabla V(\mathbf{r}) \times \sigma) \cdot \mathbf{P}. \tag{1}$$

Here m_0 is the free electron mass, **P** is the momentum operator, e is the electronic charge, σ=($\sigma_x, \sigma_y, \sigma_z$) is the vector of Pauli matrices, V(**r**) is the potential energy and ∇ stands for spatial gradient. In nanostructures depending on the origin of potential gradient,$\nabla V(\mathbf{r})$, the SO interaction in eq. (1) is known by various names. In semiconductor nanostructures without structural asymmetry the most important contribution to the potential gradient is due to the presence of impurities, as in metal films, we call this, *impurity induced spin-orbit interaction*, also known as Elliot–Yafet SO interaction [2]. In a two-dimensional electron gas, the combined effect of the impurity induced spin-orbit coupling and of a structural asymmetry of the stack with respect to the plane parallel to the layers results in an effective SO interaction known as Rashba effect [6]. This effect can be controlled by an external gate voltage [7]. It is used in the spin transistor proposed by Datta and Das [8], which is one of the paradigms of the field of spin-electronics [1].

The present paper is devoted to studying the influence of the Elliot–Yafet SO coupling and Rashba SO coupling on various phenomena of spin-dependent transport.

In §2 we introduce the Hamiltonian and derive the corresponding tight-binding Hamiltonian for the impurity induced SO interaction (Elliot–Yafet) and Rashba SO interaction in subsections 2.1 and 2.2 respectively [9,10]. Using the derived tight binding Hamiltonian we study the effects of SO interaction on charge and spin transport. Section 3 presents simulation results for a new method to image magnetic structures of surface with a *non-magnetic* scanning tip, using the tight-binding model derived in section 2.1. This method uses the spin-orbit interaction due to the presence of impurities. Section 4 is devoted to the spin transport in the presence of Rashba SO interaction and §5 discusses the anisotropy of conductance of a ferromagnetic-2DEG interface. Finally we conclude in §6.

2. Hamiltonian

2.1 *Tight binding Hamiltonian in the presence of impurity induced spin-orbit interaction*

In this section we derive the tight binding Hamiltonian for impurity induced spin-orbit coupling for 3D systems, including exchange interaction. We begin with the following single band Hamiltonian in continuum including spin-orbit and exchange coupling [9],

$$H = \frac{\hat{P}^2}{2m^*} + V(\mathbf{r}) + \frac{\Delta}{2}\vec{\mu}(\mathbf{r}) \cdot \vec{\sigma} + \lambda(\nabla V(\mathbf{r}) \times \vec{\sigma}) \cdot \hat{P}, \tag{2}$$

where the first two terms are the usual kinetic and potential energies while the third and fourth terms represent exchange and spin-orbit interaction, respectively, m^* is the effective mass of electron, Δ the exchange splitting (Δ=0 for non-magnetic system), λ is the spin-orbit interaction parameter, $\vec{\mu}$ a unit vector in the direction of magnetization of FMs and is given by ($\cos\phi \sin\theta$, $\sin\phi \sin\theta$, $\cos\theta$), $\vec{\sigma}$ the Pauli operator and $\hat{P}$ the momentum operator. By discretizing the above Hamiltonian on a simple-cubic lattice with onsite disorder, we obtain the following tight binding Hamiltonian with spin-orbit interaction whose strength is determined by disorder

$$H = \sum_{\mathbf{r},\sigma,\sigma'} \left(\varepsilon_{\mathbf{r}} \delta_{\sigma\sigma'} + \frac{\Delta_{\mathbf{r}}}{2} \vec{\mu}_{\mathbf{r}} \cdot \vec{\sigma}_{\sigma\sigma'} \right) c^{+}_{\mathbf{r},\sigma} c_{\mathbf{r},\sigma'} + t \sum_{\langle \mathbf{r},\mathbf{r}' \rangle \sigma} c^{+}_{\mathbf{r},\sigma} c_{\mathbf{r}',\sigma} + H_{\mathrm{SO}}, \tag{3}$$

where H_{SO} is expressed as

$$H_{\mathrm{SO}} = -i\alpha_{\mathrm{SO}} \sum_{\substack{\mathbf{r},\sigma,\sigma' \\ i,j,k,\nu\gamma}} \nu,\gamma \Delta\varepsilon_{\mathbf{r}+\gamma\mathbf{a}_k,\mathbf{r}+\nu\mathbf{a}_j} c^{\dagger}_{\mathbf{r},\sigma} c_{\mathbf{r}+\nu\mathbf{a}_j+\gamma\mathbf{a}_k} \sigma^{i}_{\sigma\sigma'} \varepsilon_{ijk}. \tag{4}$$

Here $c^{+}_{\mathbf{r},\sigma}$ is the creation operator of an electron with spin σ at site $\mathbf{r}$, $\varepsilon_{\mathbf{r}}$ the on-site energy and $\Delta\varepsilon_{\mathbf{r}+\gamma\mathbf{a}_k,\mathbf{r}+\nu\mathbf{a}_j} = \varepsilon_{\mathbf{r}+\gamma\mathbf{a}_k} - \varepsilon_{\mathbf{r}+\nu\mathbf{a}_j}$, $\mathbf{a_i}$ is the lattice basis vector along axis i, $\sigma^{i}_{\sigma\sigma'}$ denotes the Pauli matrix elements, α_{SO} is dimensionless spin-orbit parameter. The dummy indices ν and γ takes the values $\pm$. The summation $\langle \mathbf{r},\mathbf{r}' \rangle$ runs over to the nearest neighbor sites. The symbol ε_{ijk} is the Levi-Civita's totally antisymmetric tensor, where *ijk* label the three coordinate axes. The tight-binding parameters in eqs (3) and (4) are related with the parameters in eq. (2) in the following way:

$$t = -\frac{\hbar^2}{2m^* a^2}, \qquad \alpha_{\mathrm{SO}} = \frac{\lambda\hbar}{a^2}\ . \tag{5}$$

The above tight binding model includes two factors: spin-dependent band structure and spin-independent disorder. The band structure takes into account the difference in the density of states and the Fermi velocity between the two spin component in the ferromagnet. The disorder represents the structural defects in the systems and is a source of spin-orbit scattering and it takes the form of spin independent random variation in the atomic on-site energies. In the presence of disorder, spin-orbit coupling term causes hopping along the diagonal and is the source of spin-flip scattering. In this sense this model is equivalent to next-nearest-neighbor (nnn) tight-binding model, except that in the usual nnn tight-binding model, hopping amplitude to the next nearest neighbor is fixed while in our model it depends on disorder strength and the spin of electron. *Hence within this model spin-relaxation length is determined by disorder strength*. The relevant physical parameters are mean-free-path, spin-relaxation length, Fermi energy and the spin polarization of the ferromagnet at the Fermi level. The model parameters are, on-site energy, hopping energy, exchange splitting and spin-orbit coupling parameters. Physical parameters are related to the model parameters in the following way:

$$l_m = \frac{|t|}{\pi}\sqrt{\frac{\varepsilon_f}{|t|}}\frac{1}{N_{3D}(\varepsilon_f)\langle(V-V)^2\rangle_c}a, \tag{6}$$

$$l_{\mathrm{SO}} = l_m\sqrt{\frac{\tau_{\mathrm{SO}}}{\tau_m}} \equiv \frac{3l_m|t|}{2|\alpha_{\mathrm{SO}}|\varepsilon_f}, \tag{7}$$

$$P = \frac{N^{\uparrow}(\varepsilon_f)-N^{\downarrow}(\varepsilon_f)}{N^{\uparrow}(\varepsilon_f)+N^{\downarrow}(\varepsilon_f)} \equiv \frac{\sqrt{\varepsilon_f+\Delta}-\sqrt{\varepsilon_f-\Delta}}{\sqrt{\varepsilon_f+\Delta}+\sqrt{\varepsilon_f-\Delta}}, \tag{8}$$

where l_m, l_{SO}, P and ε_f are elastic mean free path, spin relaxation length, spin polarization of the ferromagnet and Fermi energy respectively. Here a is the lattice spacing and $\langle\ldots\rangle_c$ represents the configuration averaging (V is a disorder potential), other symbols have the same meaning as defined in the §3. In §3, using the above tight binding Hamiltonian, we present quantitative results to perform magnetic scanning tunneling microscopy with a two-terminal non-magnetic tip in the presence of spin-orbit coupling [9,11]. However, the model presented above is general and can be used to study any general system.

2.2 *Tight binding Hamiltonian for 2DEG in the presence of the Rashba spin-orbit interaction*

To obtain an appropriate Hamiltonian for 2DEG including Rashba SO interaction, we consider that 2DEG is lying in the *xy* plane, therefore the momentum operator in eq. (2) is restricted to the 2d *xy* plane, with this condition the continuum Hamiltonian of eq. (2) reduces to [10,12]

$$H = \frac{\hbar k^2}{2m^*} + V(x,y) + \frac{\Delta}{2}\vec{\mu}(\mathbf{r})\cdot\vec{\sigma} + \lambda_{\mathrm{R}}\cdot(\sigma_x k_y - \sigma_y k_x), \tag{9}$$

where $\lambda_{\mathrm{R}} = \lambda(\nabla V_z)$ is the Rashba SO parameter and is determined by the interfacial electric field perpendicular to the 2DEG plane, k is the momentum in the *xy* plane; σ_x,σ_y are the Pauli matrices. Tight binding model corresponding to the above Hamiltonian is obtained by discretizing eq. (9) on a square two-dimensional lattice of lattice spacing a with N_x sites in the longitudinal direction (current direction) and N_y lattice sites (will be also referred as the width of the channel) along the transverse direction [9,10,13]

$$\begin{aligned} H = & \sum_{i,j,\sigma,\sigma'}\left\{(\varepsilon_{i,j}\delta_{\sigma\sigma'} + \frac{\Delta_{i,j}}{2}\vec{\mu}_{i,j}\cdot\vec{\sigma}_{\sigma\sigma'})c^{+}_{i,j,\sigma}c_{i,j,\sigma'} + \mathrm{h.c.}\right\} \\ & + t\sum_{i,j,\sigma}\left\{c^{\dagger}_{i+1,j,\sigma}c_{i,j,\sigma} + c^{\dagger}_{i,j+1,\sigma}c_{i,j,\sigma} + \mathrm{h.c.}\right\} \\ & - \lambda_{\mathrm{SO}}\sum_{i,j,\sigma,\sigma'}\left\{-c^{\dagger}_{i+1,j,\sigma}c_{i,j,\sigma'}(i\sigma_y)^{\sigma\sigma'}\right. \\ & \qquad \left. + c^{\dagger}_{i,j+1,\sigma}c_{i,j,\sigma'}(i\sigma_x)^{\sigma\sigma'} + \mathrm{h.c.}\right\}, \end{aligned} \tag{10}$$

where i and j enumerates the sites along the x and y axis respectively. The $\lambda_{\mathrm{SO}} = \lambda_{\mathrm{R}}/2a$ is the Rashba spin-orbit coupling parameter having dimensions of energy, and can be controlled by an external applied gate voltage [7,14]. The other symbols in eq. (10) has

the same meaning as in eqs (3) and (4), except that now they are restricted to the two-dimensional space. The Rashba spin-orbit coupling, $\lambda_{\rm SO}$, causes spin splitting for $\mathbf{k} \neq 0$, $\Delta E = 2\alpha k$, which is linear in momentum and at the same time causes the spin to precess around the Rashba field, $\mathbf{B_R}(\mathbf{k}) = \lambda_{\rm R}(k_y\hat{x} - k_x\hat{y})$, with frequency $\omega = \Delta E/2\hbar$. The length over which spin precesses by an angle π is known as spin precession length ($L_{\rm sp}$) and is given by

$$L_{\rm sp} = \frac{\pi t}{\lambda_{\rm SO}} a. \tag{11}$$

Scattering from boundary or impurity changes the direction of Rashba field $\mathbf{B_R}(\mathbf{k})$ which depends on the electron wave vector and causes the electron to precess around a new direction, thus randomizing the precession process causing spin dephasing. The corresponding spin dephasing time (τ_ϕ) is $1/(\omega^2\tau_i)$, where τ_i is the scattering time. In diffusive regime τ_i is replaced by the elastic scattering time, $\tau_{\rm el}$, leading to spin relaxation length

$$L_\phi = \sqrt{(1/2)v_f^2\tau_{\rm el}\tau_\phi} = L_{\rm sp} \tag{12}$$

which is independent of mean free path (note that for impurity induced SO scattering, presented in section 2.1 the spin-relaxation length given by eq. (8) depends on mean free path). However, in the presence of strong disorder when the spin precession length $L_{\rm sp}$ is much larger than the mean free path L_e the spin relaxation length can show deviation from the relation given in eq. (12). We report numerical calculation in §4 which shows these deviation. The mean free path in two-dimension in the presence of Anderson onsite disorder with width W, within Born approximation is given by

$$L_e = \frac{12\hbar v_f}{2\pi N_{2d}(E_f)W^2} a, \tag{13}$$

where $N_{2d}(E_f)$ is the density of states. Here we would like to remind the reader that in 2D tight binding model, density of states are singular in the middle of the band, and goes to a constant near the band edge. This effects the mean free path drastically in the band center and can lead to a non-monotonic behavior for spin coherence as a function of Fermi energy as we will see in §4.

3. Magnetic scanning tunneling microscopy with a non-magnetic tip: An effect of impurity induced spin-orbit coupling

Imaging the magnetic structures of surfaces down to the atomic level is a major goal of surface magnetism. Magnetic scanning tunneling microscopy (MSTM) provides a way to image magnetic domains on the surface. In the conventional approach magnetic sensitivity of tunneling current has been based upon the spin-valve effect [15], the tunneling current between two ferromagnets separated by a tunnel barrier depend on the relative orientation of the magnetizations of the ferromagnets. In this approach a magnetic tip has to be used. The experimental realization of magnetic scanning tunneling microscopy based on spin-valve effect was realized by Wiesendanger *et al* [16], who investigated a Cr(001)

surface with a ferromagnetic CrO_2 tip, their observation confirmed the model of topological antiferromagnetism between ferromagnetic terraces separated by monoatomic steps. They measured a spin asymmetry of the order of 20%. Recently this method has been used to image magnetic domains [17–20]. It was shown that, by periodically changing the magnetization of the tip, it is possible to separate spin-dependent tunnel current from the topographic dependent current and hence the magnetic structure of the surface can be recorded. Using this method Wulfhekel *et al* [17] studied magnetic domain structure on a single crystalline Co(0001) surface and polycrystalline Ni surface. In refs [18–20], a two-dimensional anti-ferromagnetic structure of Mn atoms on tungsten(110) surface was investigated. It was shown that the spin-polarized tunneling current is sensitive to the magnetic superstructure, and not to the chemical unit cell [18].

However, the MSTM with a magnetic tip has a drawback that the magnetostatic interaction between the tip and magnetic sample cannot be avoided, which are likely to influence the domain structure. In view of this an alternative approach was recently proposed to perform the magnetic scanning tunneling microscopy with a two-terminal non-magnetic tip [11]. It is based upon Mott's spin-asymmetry effect in scattering caused by disorder [21]. It was shown that due to spin-orbit coupling the tunnel conductance between the ferromagnetic surface and one of the tip terminal depends on the orientation of magnetization. Because of the spin-orbit interaction the intensity of the scattered beam depends on the orientation of spin-polarization axis of the incidents electrons, i.e., it is sensitive to the spin component perpendicular to the scattering plane. In other words tunnel conductance is spin asymmetric. However, to observe this spin asymmetry effect, caused by Mott scattering, a three-terminal device is a prerequisite. Due to the Casimir–Onsager symmetry relation the conductance of a two-terminal device has to be symmetric with respect to magnetic field (in our case spin plays the role of magnetic field since as far as time reversal properties are concerned 'spin' and 'magnetic field are equivalent), this is a requirement imposed by the underlying microscopic time reversal symmetry. However, in the case of the three-terminal device, there is no such restriction on the conductance; rather, a more generalized symmetry relation exists involving all terminals as shown by Büttiker [22]. Hence to perform magnetization sensitive scanning tunneling microscopy with a non-magnetic tip, it is necessary to use a two-terminal tip [11].

In this section we present numerical simulation results of the three-terminal STM device within the single-band tight-binding model introduced in section 2.1, using recursive Green function method and Landauer–Büttiker formula for conductance [9].

A cross-section of the system in the *xy* plane, for the calculation of spin sensitivity of the proposed two-terminal non-magnetic tip is shown in figure 1. The system consists of three regions: (i) the ferromagnetic lead (labelled 1 in figure 1), (ii) the central region and, (iii) the two non-magnetic terminals (labelled as 2 and 3 in figure 1). The central region is composed of an insulating tip, such as those routinely used to perform atomic force microscopy, coated on two opposite faces by a thin metallic film. The metallic coating has a thickness *d*. This is shown in the central region where the empty circles depict vacuum, black circles corresponds to insulating sites and the rest corresponds to metallic sites (hatched circles) and the impurities (stars). Between the ferromagnetic surface (gray circles in figure 1) and the tip there is a vacuum layer of one lattice spacing (empty circles in figure 1). The tip is placed symmetrical with respect to the *xz* plane. Current flows along the two faces of the tip which makes an angle of $\pm 45^\circ$ with the x-axis. The structure shown in figure 1 consists of three semi-infinite leads ($-\infty \leq i \leq 1$ and $N_x + 1 \leq i \leq \infty$)

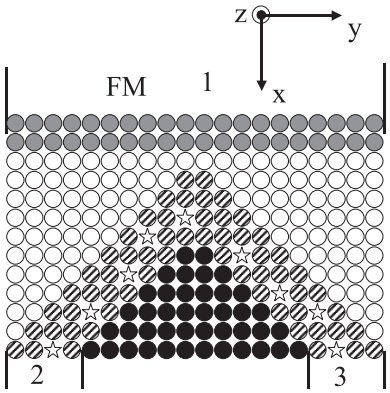

Figure 1. Cross-section of tip-geometry shown in *xy* plane. Gray circles denote ferromagnetic sample, the empty circles depict vacuum, black circles corresponds to insulating sites and the rest corresponds to metallic sites (circles with downward diagonal lines) and the impurities (empty stars) in the tip.

separated by the tip region $1 \leq i \leq N_x$. The thickness of the metallic coating on the tip is da where a is the lattice constant and the cross-section of the system is $(N_y a \times N_z a)$, where N_y and N_z are the number of sites along y- and z-axes. For numerical calculation we have taken $N_y = N_z = 20$, $N_x = 10$ and the metallic coating on the tip has a thickness of 4 lattice spacing, i.e., $d = 4$ as shown in figure 1 [22,23].

As shown in figure 1, in the ferromagnet, the left face of the tip and the right face of the tip is connected to three reservoirs at chemical potentials V_1, V_2 and V_3 respectively. Let I_1, I_2 and I_3 be the corresponding incoming currents in the three terminals. The currents are related to potentials by

$$I_p = \sum_{q \neq p} G_{pq}(V_p - V_q). \tag{14}$$

The above expression is gauge invariant and the currents conservation law $\sum_i I_i = 0$ requires that $G_{pq} = G_{qp}$ be satisfied.

The calculation of the conductance of the structure is based on the non-equilibrium Green's function formalism [24,25]. When applied to multi-terminal ballistic mesoscopic conductor we obtain the following result for the conductance [23]

$$G_{pq} = \frac{e^2}{h} \mathrm{Tr}[\Gamma_q G^{\mathrm{R}} \Gamma_p G^{\mathrm{A}}]. \tag{15}$$

Here p and q enumerates the three terminals and the upper indices R and A refer to the retarded and advanced Green function of the whole structure taking leads into account. Here $\Gamma_{p(q)}$ self-energy function for the isolated ideal leads are given by $\Gamma_{p(q)} = t^2 A_{p(q)}$, where $A_{p(q)}$ is the spectral density in the respective lead when it is decoupled from the structure. The trace is over space and spin degrees of freedom, and all the matrices in

eq. (4) are of size $(2N_y \times N_z, 2N_y \times N_z)$, where N_y and N_z are the number of sites along the y and z direction and the factor 2 takes into account the spin degree of freedom. All the quantities in the above equations are evaluated at the Fermi energy. To calculate the required Green function we use the well-known recursive Green function method [26].

We present numerical results for a system of cross-section (20×20) in yz plane and a length of 10 lattice spacing along the x direction. The number of metallic layers on the tip, i.e., d in figure 1 is taken to be 4 lattice spacings. The hopping parameter, t, is same for all pairs and set to -1 for numerical calculation. The on-site energies in the leads and on the metal coating on the tip is set to be zero, while in the vacuum layer it is $\varepsilon_{\text{vac}} = 4.0|t|$, and in the tip of the insulating region it is $\varepsilon_{\text{ins}} = 10.0|t|$. The Fermi level throughout the calculation is kept fixed at $\varepsilon_f = 3|t|$ above the bottom of the band. For disorder we consider Anderson model in which a random on-site energy, characterized by square distribution of width W, is added to the on-site energy of perfect case. In our case disorder is added only in the metallic coating on the tip; everywhere else the system is perfect.

In figure 2 we have plotted the conductance G_{12} and G_{13} as a function of magnetization angle θ with respect to the z axis. We rotate the magnetization in the yz plane such that the magnetization is always perpendicular to the x-axis or in other words the angle ϕ does not change and has a fixed value of 90°. To be specific, when $\theta = 0$ and $\phi = 90^\circ$, magnetization is parallel to the z-axis while for $\theta = 90^\circ$ and $\phi = 90^\circ$ the magnetization is parallel to the y-axis. We have taken $\varepsilon_f = 3|t|$, $\alpha_{\text{SO}} = 0.02$ and $\Delta = 2.4|t|$ and the Anderson disorder strength is $W = 1|t|$.

This set of parameters corresponds to a mean free path of $l_m = 80a$, spin relaxation length of $l_{\text{SO}} = 25l_m$ and polarization is $P = 50\%$. We notice that the conductance shows approximately $\cos(\theta)$ as a function of angle, which is expected since in our geometry the tip is placed symmetrically to xz plane. However, because of disorder the effective axis in the system does not coincide with the chosen spin quantization

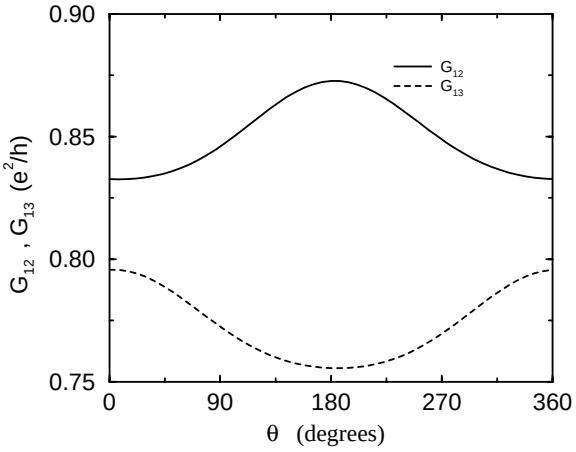

Figure 2. Conductance (G_{12} and G_{13}) versus θ plot for the two terminals for a fixed value of $\phi = 90$. The other parameters chosen for this figure are $\varepsilon_f = 3.0|t|$, $\Delta = 2.4|t|$, $\alpha_{\text{SO}} = 0.02$, and $W = 1|t|$.

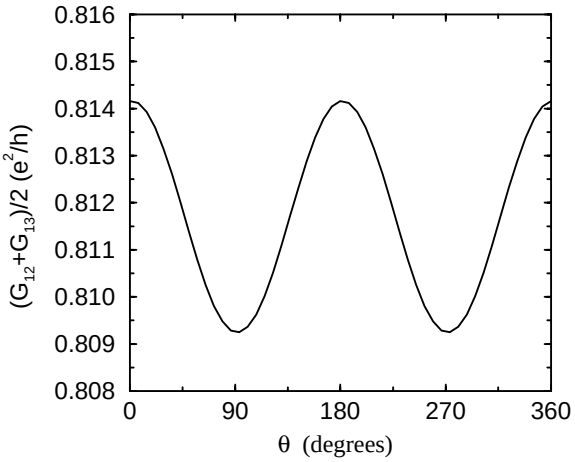

Figure 3. Plot of the average two-terminal conductance $(G_{12}+G_{13})/2$ versus θ. The other parameters are same as those in figure 2.

axis, i.e., z axis, and also since the structure considered is three-dimensional the scattering plane is not fixed and hence the conductance variation with magnetization angle does not show an exact cosine behavior. Also we notice that the variation of G_{13} is opposite to that of G_{12}. This is in agreement with the underlying microscopic time-reversible symmetry which requires that the two-terminal conductance should be symmetric under time reversal.

To verify this point in figure 3 we have plotted the sum of $(G_{12}+G_{13})/2$. We see that the two-terminal conductance is symmetric with respect to magnetization angle θ and also the magnitude of oscillation is much smaller than either G_{12} or G_{13}. This is due to the fact that the variation of G_{12} or G_{13} with θ is of first-order with respect to the spin-orbit coupling, whereas the variation of $G_{12}+G_{13}$ is of second order with respect to spin-orbit coupling. Actually the latter can be viewed as related to the anisotropic magnetoresistance of ferromagnets, whereas the former is related to the extraordinary Hall effect. In fact from this figure it is clear that the conductance of a ferromagnetic–nonmagnetic interface will be anisotropic in the presence of spin-orbit coupling [10]. The essential point here is that the conductance of a ferromagnetic-nonmagnetic interface, in the presence of SO interaction depends on the magnetization angle of ferromagnet and is consistent with the Büttiker symmetry relation [22]. This anisotropy exist irrespective of the dimensionality of the system considered as we will see later in §5.

In figure 4 we plot spin asymmetry as a function of polarization of ferromagnet for the terminal 2. We have defined the spin-asymmetry as

$$A = \frac{G_{12}^{\max} - G_{12}^{\min}}{G_{12}^{\max} + G_{12}^{\min}}, \tag{16}$$

where to find $G_{12}^{\max}$ and $G_{12}^{\min}$ we generate a curve as shown in figure 3 for each set of parameters and from these points we get the corresponding maximum and minimum values. This is necessary since the variation of conductance with magnetization angle does

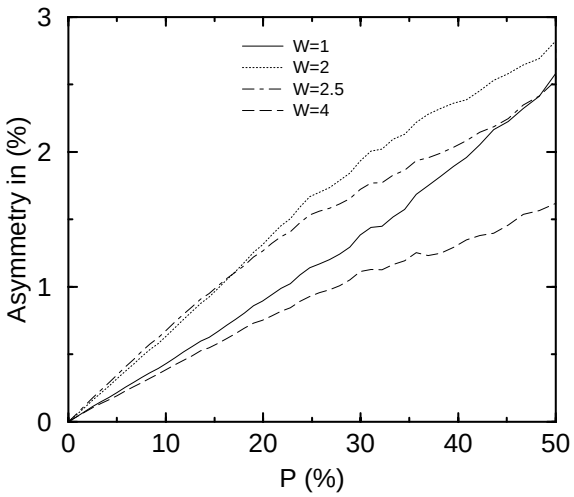

Figure 4. Spin asymmetry A as a function of polarization for different disorder strength. The other parameters are $\varepsilon_f = 3.0|t|$ and $\alpha_{\mathrm{SO}} = 0.02$.

not follow exact cosine behavior, the maxima and minima need not occur exactly at zero and π respectively. We have fixed Fermi energy at $\varepsilon_f = 3|t|$ and $\alpha_{\mathrm{SO}} = 0.02$. Different curves in figure 4 correspond to disorder strengths $W = 1|t|$ (solid line), $W = 2|t|$ (dotted line), $W = 2.5|t|$ (dot–dashed line) and $W = 4|t|$ (dashed line) whose corresponding mean-free-paths are respectively $80a$, $10a$, $6a$, and $3a$. Although all these curves correspond to different mean-free-paths, the ratio l_{SO}/l_m is the same for all the curves and is equal to 25, since this ratio is determined by Fermi energy and spin-orbit coupling strength, which are kept fixed here.

We see that for a fixed disorder strength the spin asymmetry increases linearly with the polarization or in other words spin asymmetry is directly proportional to the polarization of ferromagnet. However, for a fixed polarization value, spin asymmetry shows a non-monotonic behavior. As we increase disorder strength, spin asymmetry first increase and then starts decreasing. This shows that the spin asymmetry is maximum when the system is in quasi-ballistic regime, since the multiple scattering destroys the spin asymmetry effect. This is clearly visible in figure 4 where spin asymmetry is maximum, for a fixed value of polarization, at a disorder strength $W = 2|t|$, corresponding to a mean-free-path of $10a$, while it is minimum for $W = 4|t|$ corresponding to a mean-free-path of $3a$ lattice spacings. The order of magnitude of spin asymmetry is 5%, which is in good agreement with the prediction in ref. [11].

In figure 5 we have studied the behavior of spin asymmetry as a function of spin-orbit coupling parameter α_{SO}. The other parameters are same as in figure 4. We notice that the spin asymmetry shows a linear behavior for small values of $\alpha_{\mathrm{SO}} \leq 0.03$. For larger α_{SO} the linear behavior is no longer seen because for a fixed disorder, i.e., fixed l_m, as we increase α_{SO}, correspondingly, l_{SO}, i.e. spin-relaxation path decreases, hence the higher order effect in spin-orbit coupling starts dominating so we no longer observe a linear behavior. Also we see that for a fixed α_{SO}, spin asymmetry shows a maximum at a disorder strength of around $W = 2|t|$. This is in harmony with the results presented in figure 4. A typical value

of spin asymmetry is of the order of 5%. So from the results of figures 4 and 5 we can say with confidence that the efficiency of the proposed three-terminal STM device would be maximum when the device operates in quasi-ballistic regime.

In summary we have developed a new model to take into account spin-orbit scattering within the single-band tight-binding model. Using this model we have done numerical calculations of MSTM with a non-magnetic tip. The order of magnitude of the spin asymmetry is about 5%, which is in good agreement with the qualitative estimate given in [11], and the effect is maximum when the device operates in the quasi-ballistic regime. The spin asymmetry of the present effect is smaller than the one obtained in the spin-valve tunneling structures. However, it has some advantages. In particular since the tip is non-magnetic, it is insensitive to an external magnetic field. This allows one to study the domain structure as a function of applied field. Furthermore, the problem of the magnetostatic interaction between the tip and the magnetic sample is avoided, which in case of a magnetic tip would give rise to undesirable magnetic forces between the tip and the sample and are likely to influence the domain structure. Another important advantage of this technique is that by measuring separately the currents I_2 and I_3 of the two-tip terminals, and by combining them appropriately, one can separate the weak magnetic contrast from the dominant topographic contrast: the sum $I_2 + I_3$ depends only on the topography, whereas the magnetic information is contained in the difference $I_2 + I_3$. Besides all these advantages it has an intrinsic limitation that only in-plane components can be studied and also since multiple scattering diminishes the spin-asymmetry effect, it is necessary that the device operates in a quasi-ballistic regime. However, to construct such a tip would be experimentally challenging.

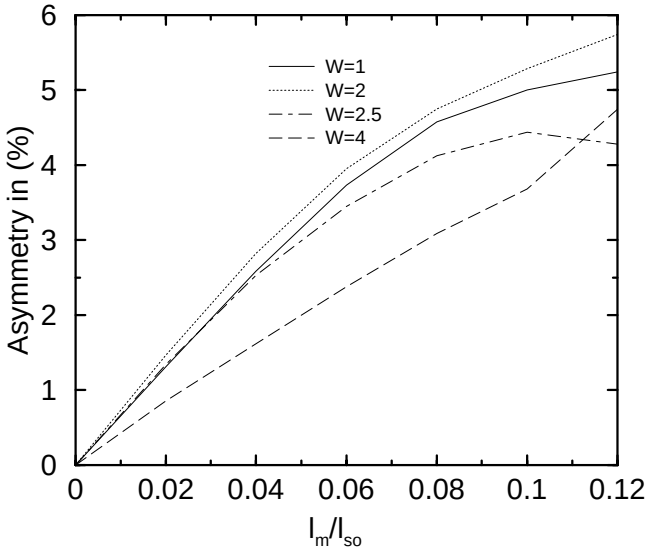

Figure 5. Spin asymmetry A, as a function of l_m/l_{SO} for different disorder strength. The other parameters are $\varepsilon_f = 3.0|t|$ and $\Delta = 2.4|t|$. Corresponding value of polarization is 50%.

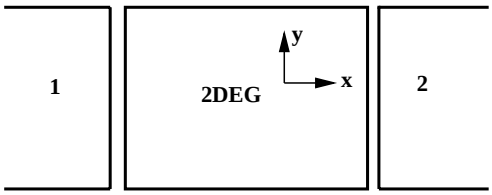

Figure 6. A 2DEG lying in *xy* plane connected to two semi-infinite ideal leads.

4. Spin transport in two-dimensional electron gas in the presence of Rashba spin-orbit interaction

In this section we present a study of spin coherence in 2DEG in the presence of Rashba SO interaction using the tight binding Hamiltonian presented in section 2.2. We consider a system 2DEG lying in *xy* plane as shown in figure 6, with N_x sites along the *x*-axis (the current direction) and with N_y (will also be referred as the width of the channel) sites along *y*-axis, i.e., transverse direction perpendicular to the current direction. The 2DEG is connected to two ideal non-magnetic leads 1 and 2 as shown in figure 6.

Though the injected current is unpolarized, by analyzing the spin-resolved conductance for a given quantization axis we can infer the information about spin coherence. To this end we calculate spin resolved conductances using Landauer–Büttiker [22] formalism as presented in eq. (15). The two terminal spin resolved conductance (for a given spin quantization axis) is given by [10]

$$G^{\sigma\sigma'}(\varepsilon_{\mathrm{F}}) = \frac{e^2}{h}\mathrm{Tr}[\Gamma_1^{\sigma} G_{1N_x}^{\sigma\sigma'} \Gamma_{N_x}^{\sigma'} G_{N_x 1}^{\sigma'\sigma -}], \tag{17}$$

where the symbols have the same meaning as defined in eq. (15). The trace is over spatial degrees of freedom. The total conductance is the sum of spin-spin conserved conductance and spin-flip conductance, i.e., $G = G_{\mathrm{sc}} + G_{\mathrm{sf}}$ where the spin-spin conserved and spin-flip conductance are $G_{\mathrm{sc}} = G^{\uparrow\uparrow} + G^{\downarrow\downarrow}$ and $G_{\mathrm{sf}} = G^{\uparrow\downarrow} + G^{\downarrow\uparrow}$ respectively. We point out that in our simulation the injected current is unpolarized since the ideal leads are non-magnetic. However by analyzing the spin resolved conductances we can study the spin coherence phenomena which would be observable when the injector and the detector are magnetic.

Figure 7 depicts the conductance and spin resolved conductance for different spin quantization axis as a function of length along the *x*-axis, i.e., current direction. The behavior of spin resolved conductance is different for different quantization axis since the system considered here is confined along transverse *y* direction and the effective Rashba field $\mathbf{B}_{\mathbf{R}}(\mathbf{k})$ is almost parallel to the *y*-axis. Hence the spin polarization does not show the oscillation, for the case (lower panel in figure 1) when the spin quantization axis is along the *y*-axis. We note that the spin coherence length (L_ϕ) is three times larger than the spin precession length (L_{sp}) (in figure 6 the point where the difference between G_{sc} and G_{sf} tends to zero). Since the mean free path (122a) and the spin precession length (104a) are of the same order, this regime corresponds to large elementary rotation during electron free flight, but still spin coherence length is longer than the spin precession length. An appropriate quantity which is suitable to study spin coherence is polarization of the transmitted electrons, defined as

$$P = \frac{G_{\rm sc} - G_{\rm sf}}{G_{\rm sc} + G_{\rm sf}}. \tag{18}$$

From the definition it is clear that the polarization lies strictly between $+1$ (spin conserved) and -1 (spin flip). The polarization corresponding to figure 1 is shown in figure 8. We see that polarization is always positive for spin quantization axis *y* while for spin quantization axis *x* and *z*, it shows oscillation of larger amplitude. The amplitude of oscillation is different for *x* and *z* direction. This implies that for Datta–Das [8] spin transistor a larger current

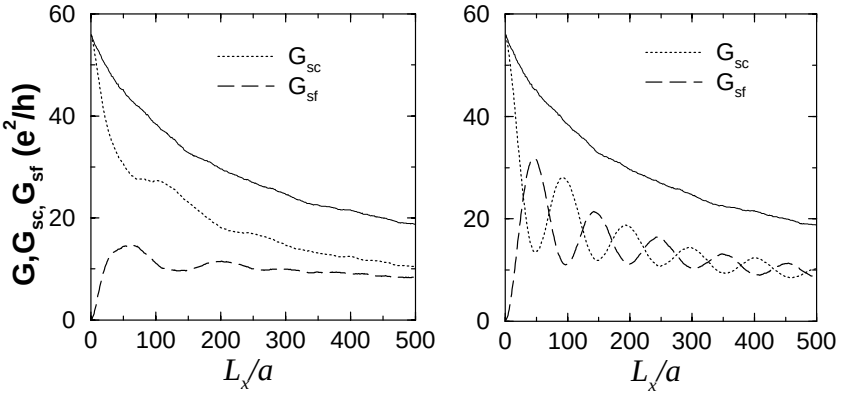

Figure 7. Conductance (_____), spin conserved conductance (- - -) and spin flip conductance ($\cdots$) as a function of channel length. Left panel spin quantization axis is *y*-axis, for right panel *x*-axis, channel width is 80. The model parameters are $E_f = 1.1t$, $W = 0.5|t|$, and $\lambda_{\rm SO} = 0.03|t|$.

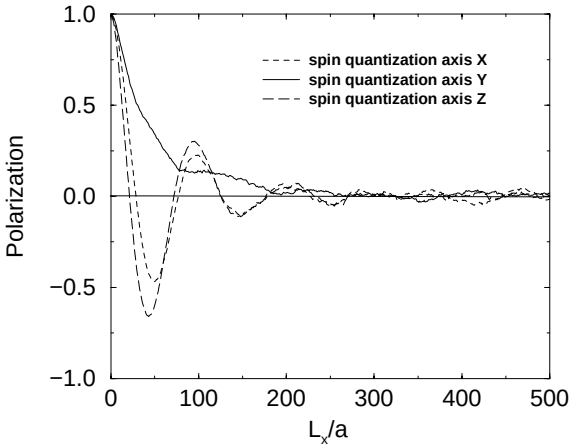

Figure 8. Polarization as function of channel length, parameters for this fig is same as those for figure 1.

modulation will be obtained as a function of gate voltage when the magnetization direction of injector-detector ferromagnets are parallel to the current direction.

Figure 9 illustrates the point that in the diffusive regime to preserve spin coherence one need to confine electrons to a width of the order of mean free path and not to tens of mean free path as claimed by real space Monte Carlo simulation [28]. The mean free path for figure 3 is 30a. We see that the polarization for channel width 30a, 50a and 80a decays much faster as a function of channel length compared to the channel width 10a and 20a, which is less than the mean free path. This shows a cross over from quasi-ballistic regime to diffusive regime. Also the polarization remains almost unchanged corresponding to channel width 10a, which is consistent with the 1D limit exhibiting no spin decoherence, since all rotations are along one axis and are commuting [29].

The results presented above were in the regime where the mean free path and spin precession lengths were such that during free flight electrons spin precession was of finite value. However, the other regime of small precession during electron's free flight can give rise to qualitatively different results as seen in figure 10, where we have plotted polarization for spin quantization axis *y* for different mean free paths keeping the spin precession length fixed. This is the regime where ($l_{\rm mfp} \ll L_{\rm sp}$ or $L_{\rm sp}/L_e \gg 1$), so that during its free flight electron polarization precesses by a small angle. As we reduce mean free path while keeping spin precession length fixed we observe an enhancement of spin coherence, or in other words polarization decay is suppressed, i.e. disorder helps to preserve spin coherence. Note the opposite behavior for $\lambda_{\rm SO} \geq 0.02$. This is the regime of finite precession during free flight and disorder reduces spin polarization which is opposite to the behavior for small precession regime. However, for large values of $\lambda_{\rm SO} \geq 0.1$, spin polarization increases as seen in the right panel.

Thus encouraged by the results we study the spin coherence as a function of Fermi energy. Motivation comes from the simple observation that the mean free path in two

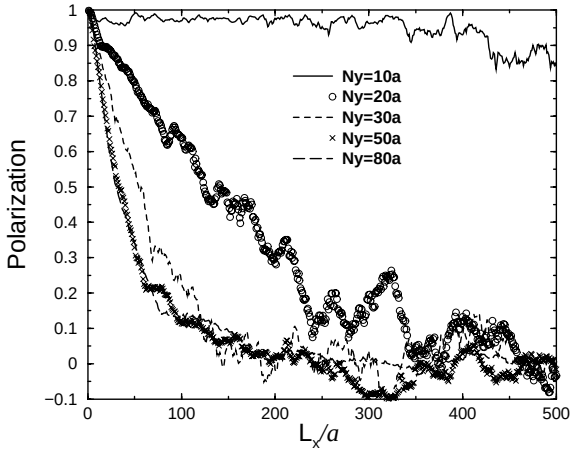

Figure 9. Polarization as a function of channel length for different channel width. Mean free path and spin precession length are 30a and 104a ($\lambda_{\rm SO} = 0.02|t|$) respectively. The other parameters are same as those for figure 1.

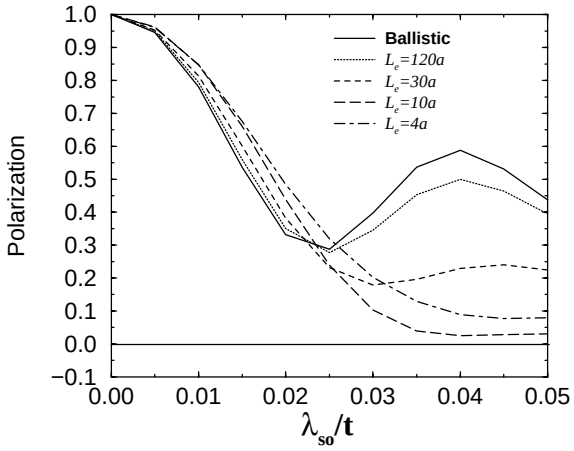

Figure 10. Polarization as a function of Rashba spin-orbit coupling parameter. Different curves corresponds to different mean free path as shown in the figure. The system size is 80×80.

dimension behave like $L_e \approx \sqrt{(E_f)}/(N_{2d}(E_f)W^2)$, any deviation from non-parabolicity in the band will affect the density of states and therefore the spin coherence. Near the band edges, where energy band can be well-approximated by parabola, the mean free path increases as Fermi energy is increased since $N_{2d}(E_f)$ is constant. However as one approaches the band center, $N_{2d}(E_f)$ start to diverge logarithmically within 2d tight binding model (Von Hove singularity). This in turn causes mean free path to decrease. This is due to non-parabolicity of the energy band and in recent experiments by Hu *et al* [14], it was reported to cause a reduction in Rashba spin-orbit coupling $\lambda_{\rm SO}$ by 25%. The reduction in $\lambda_{\rm SO}$ due to non-parabolicity is encouraging since it will increase the spin precession length which can only help to push the parameters in the regime of small precession. From the discussion above we see that as we move away from the band edges, initially mean free path will increase and then starts to decrease, and will be shortest at the band center. Though the presence of disorder will weaken the singularity in the density of states, it still remains peaked at the band center as reported recently in ref. [32]. Hence we expect that for any value of spin precession length, the band center will always correspond to the regime of small precession and therefore the enhancement of spin coherence, i.e., polarization should be maximum at the band center.

This is clearly seen in figure 11, where we have plotted polarization as a function of Fermi energy for different strength of disorder, where $\lambda_{\rm SO} = 0.02$ or the equivalent spin-precession length is $L_{\rm sp} = 157a$. We notice that in the middle of the band polarization enhancement is largest compared to the ballistics case even for the weak disorder, i.e, $W/t = 0.5$ and 1.0. This is in agreement with the fact that density of states are peaked at band center [32]. Also it is seen that polarization for $W/t = 0.5,\ 1.0$ and 2.0 decreases till $|E_f| \approx 2.0$ (measured from the band edge) and beyond this point increases in disorder strength always enhances the polarization. In the energy window $-2 \leq E_{\rm F} \leq 2$ we are always in the regime of small rotations i.e., $L_{\rm sp}/L_e \gg 1$. Hence polarization is enhanced compared to ballistic case irrespective of the disorder strength. Beyond $-2 \leq E_f \leq 0$ the

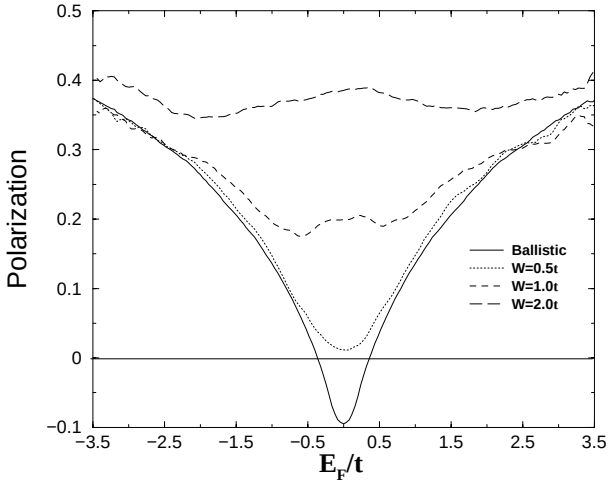

Figure 11. Polarization as a function of Fermi energy in units of $|t|$. Different curves corresponds to different values of disorder strength W. The system size is 80×80. The Rashba spin-orbit coupling $\lambda_{SO} = 0.02$, corresponding spin precession length is 157a. Disorder averaging was performed for 20 different realization for each W.

curve for $W/t = 2.0$ shows an increase in polarization. This is expected since an increase in disorder only helps to decrease the mean free path. This is in agreement with the results presented earlier. So from this curve we can safely draw the conclusion that as we move away from the band edge, polarization will decrease initially and then will start to increase again till the band center, i.e. polarization shows a non-monotonic behavior as a function of Fermi energy. This is the coupled effect of disorder and non-parabolicity of energy band. This non-monotonic behavior should be seen with reference to the recent experiment on *n*-type GaAs [33], where observed spin life-time show a non-monotonic behavior as a function of carrier density. In this experiment carrier density was controlled through doping, which increases the Fermi energy and reduces the mean free path. Therefore, our result might provide a qualitative explanation for the said experiment. Another interesting conclusion which can be drawn from figure 11 is, the diffusive case spin coherence can be preserved even for wide channels, since disorder helps to preserve spin coherence as soon as non-parabolicity of density of states starts to play a role, however weak the disorder may be. This is clearly illustrated in figure 11 where all the curves in the presence of disorder lies above the curve for ballistic case in the range $-2 \leq E_f \leq 2$. This might have an important implication for Datta–Das spin transistor [8], since it removes the stringent criterion to confine electrons in one dimension.

5. Symmetry and anisotropy of conductance of a ferromagnetic-2DEG interface

In this section we consider the following question: Does the conductance of a FM/2DEG interface depend on the magnetization direction? Büttiker symmetry relation for electrical conduction says that when one flips the magnetization of the ferromagnet, conductance

should remain invariant. However, it does not make any statement about how conductance should behave when one changes the direction of magnetization. Motivated by this and the recent erroneous claim in ref. [34], where it was claimed that the conductance of FM/2DEG interface changes upon the flip of magnetization direction, which is obviously incorrect in the light of the Büttiker symmetry relation, we present the results for the conductance of FM/2DEG interface and point out that the conductance is anisotropic [10]. The results are shown in figure 12, as is seen clearly when we rotate the magnetization direction in the *yz* plane the conductance changes, and the conductance curve is symmetric with the magnetization angle which is consistent with the Büttiker symmetry relation. This anisotropy exist even for 3D systems with impurity induced spin-orbit interaction as shown in figure 3. This is in contrast to the result of ref. [35] where they used effective mass Hamiltonian presented in eq. (9) and showed that conductance of a FM/2DEG interface is invariant upon the rotation of magnetization. It was argued in ref. [35] that the anisotropy which is seen in numerical simulation within tight binding model is a consequence of reduced symmetry of lattice. However we believe that the anisotropy is due to the simultaneous presence of exchange and spin-orbit interaction, though they are spatially separated. The existence of anisotropy is due to the presence of SO interaction which breaks rotational invariance in space.

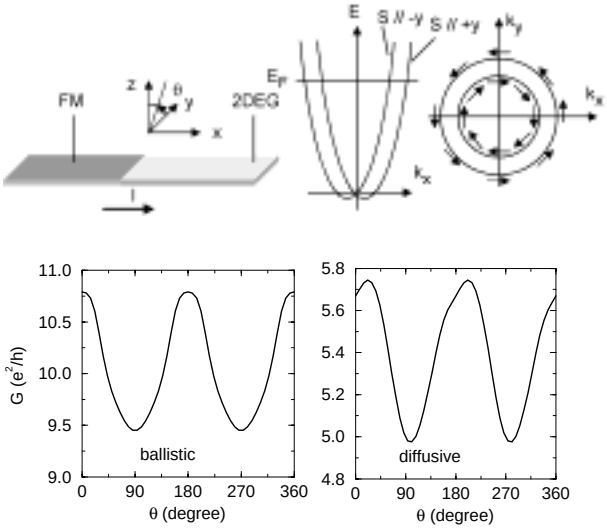

Figure 12. Top: schematic description of the device geometry (left), and of the band-structure (center) and Fermi surface (right) of a 2DEG with Rashba effect; the arrows indicate the direction of the spin-quantization axis. Bottom: Two-terminal conductance of a FM/2DEG junction as a function of the angle θ of the magnetization in *yz* plane for the ballistic (left) and diffusive (right) cases. Calculations were performed on a 50×50 lattice with $k_F a = 1$, FM exchange splitting Δ given by $\Delta/\varepsilon_F = 0.5$, 2DEG Rashba parameter $k_F\alpha/\varepsilon_F = 0.03$; for the diffusive case (no configuration averaging), the mean-free-path l is given by $k_F l = 30$.

6. Conclusion

In summary we have presented new single band tight binding model including Elliot–Yafet and Rashba SO interaction. Using these tight binding models effect of SO interaction on spin and charge transport is studied. Numerical results were presented for spin relaxation in 2DEG in the presence of Rashba SO interaction and it was shown contrary to naive expectation that disorder helps to reduce spin relaxation. Also it is pointed out that conductance of a FM/2DEG interface can be anisotropic due to the simultaneous presence of exchange and SO interaction.

References

[1] G Prinz, *Phys. Today* **48**, 58 (1995)

[2] R J Elliot, *Phys. Rev.* **96**, 266 (1954)
Y Yafet, in *Solid state physics* edited by F Seitz and D Turnbull (Academic, New York, 1963) vol. 14

[3] M I D'yakonov and V I Perel', *Sov. Phys. JETP* **33**, 1053 (1971); *Sov. Phys. Solid State* **13**, 3023 (1972)

[4] A G Aronov, G E Pikus and A N Titkov, *Sov. Phys. JETP* **57**, 680 (1983)

[5] J Fabian and S Das Sarma, *J. Vac. Sci. Tech.* **B17**, 1708 (1999)

[6] Yu A Bychkov and E I Rashba, *Sov. Phys. JETP Lett.* **39**, 78 (1984)

[7] G Lommer, F Malcher and U Rössler, *Phys. Rev. Lett.* **60**, 728 (1988)
B Das, S Datta and R Reifenberger, *Phys. Rev.* **B41**, 8278 (1990)
J Nitta, T Akazaki, H Takayanagi and T Enkoi, *Phys. Rev. Lett.* **78**, 1335 (1997)
J P Heida, B J van Wees, J J Kuipers, T M Klapwijk and G Borghs, *Phys. Rev.* **B57**, 11911 (1998)
G Engels, J Lange, Th Schäpers and H Lüth, *Phys. Rev.* **B55**, 1958 (1997)
D Grundler, *Phys. Rev. Lett.* **84**, 6074 (2000)
T Matsuyama, R Kürsten, C Messner and U Merkt, *Phys. Rev.* **B61**, 15588 (2000)

[8] S Datta and B Das, *Appl. Phys. Lett.* **56**, 665 (1990)

[9] T P Pareek and P Bruno, *Phys. Rev.* **B63**, 165424-1 (2001)

[10] T P Pareek and P Bruno, submitted for publication

[11] P Bruno, *Phys. Rev. Lett.* **79**, 4593 (1997)

[12] P Bruno and T P Pareek, cond-mat/0105506

[13] F Mireles and G Kirczenow, *Phys. Rev.* **B64**, 024426 (2001)

[14] C-M Hu, J Nitta, T Akazaki, H Takayanagi, J Osaka, P Pfeffer and W Zawadski, *Phys. Rev.* **B60**, 7736 (1999)

[15] M Juliere, *Phys. Lett.* **A54**, 225 (1975)
S Maekawa and U Gäfvert, *IEEE Trans. Magn.* **18**, 707 (1982)
J C Slonczewski, *Phys. Rev.* **B39**, 6995 (1989)

[16] R Wiesendanger, H J Güntherodt, G Güntherodt, R J Gambino and R Ruf, *Phys. Rev. Lett.* **65**, 247 (1990)
R Wiesendanger, *J. Magn. Soc. Jpn.* **18**, 4 (1994)

[17] W Wulfhekel and J Kirschner, *Appl. Phys. Lett.* **75**, 1944 (1999)

[18] S Heinze, M Bode, A Kubetzka, O Pietzsch, X Nie, S Blügel and R Wiesendanger, *Science* **288**, 1805 (2000)

[19] O Pietzsch, A Kubetzka, M Bode and R Wiesendanger, *Phys. Rev. Lett.* **84**, 5212 (2000)

[20] M Bode, M Getzlaff and R Wiesendanger, *Phys. Rev. Lett.* **81**, 4256 (1998)

[21] N F Mott, *Proc. R. Soc. London* **A124**, 438 (1929)
[22] M Büttiker, *Phys. Rev. Lett.* **57**, 1761 (1986); *IBM J. Res. Dev.* **32**, 317 (1988)
[23] S Datta, *Electronic transport in mesoscopic systems* (Cambridge University Press, Cambridge, 1995)
[24] L P Kadanoff and G Baym, *Quantum statistical mechanics* (Benjamin, New York, 1962)
[25] L V Keldysh, *Sov. Phys. JETP* **20**, 1018 (1965)
[26] H U Baranger, D P DiVincenzo, R A Jalabert and A D Stone, *Phys. Rev.* **B44**, 10637 (1991)
[27] G L Chen, J Han, T T Huang, S Datta and D B Janes, *Phys. Rev.* **B47**, 4084 (1993)
[28] A A Kiselev and K W Kim, *Phys. Rev.* **B61**, 13115 (2000)
[29] A Bournel, P Dollfus, P Bruno and P Hesto, *Eur. Phys. J. Appl. Phys.* **4**, 1 (1998); *Physica* **B4**, 272 (1999)
[30] A G Mal'shukov and K A Chao, *Phys. Rev.* **B61**, R2413 (2000)
[31] H X Tang, F G Monzon, Ron Lifshtiz, M C Cross and M L Roukes, *Phys. Rev.* **B61**, 4437 (2000)
[32] Y Avishai and Y Mier, cond-mat/0107591
[33] J M Kikkawa, I P Smorchkova, N Samarth and D D Awschalom, *Science* **277**, 1284 (1997)
J M Kikkawa and D D Awschalom, *Phys. Rev. Lett.* **80**, 4313 (1998)
[34] D Grundler, *Phys. Rev. Lett.* **86**, 1058 (2001)
[35] L W Molenkamp, G Schmidt and G E W Bauer, cond-mat/0104109